Effect of hydriding induced defects on the small-scale plasticity mechanisms in nanocrystalline palladium thin films

Gunnar Lumbeeck[1], Hosni Idrissi[2,1], Behnam Amin-Ahmadi[3], Audrey Favache[2], Renaud Delmelle[4], Vahid Samaee[1], Joris Proost[2], Thomas Pardoen[2], Dominique Schryvers[1]

[1]Electron Microscopy for Materials Science (EMAT), Department of Physics, University of Antwerp, Groenenborgerlaan 171, B-2020 Antwerp, Belgium
[2]Institute of Mechanics, Materials and Civil Engineering, UCLouvain, Place Sainte Barbe 2, B-1348 Louvain-la-Neuve, Belgium
[3]Department of mechanical Engineering, Colorado School of Mines, 1500 Illinois St, Golden, CO 80401, USA
[4]Institute for Materials and Process Engineering (IMPE), Zurich University of Applied Sciences, Technikumstrasse 9, 8400 Winterthur, Switzerland

Abstract

Nanoindentation tests performed on nanocrystalline palladium films subjected to hydriding/dehydriding cycles demonstrate significant softening when compared to the as-received material. The origin of this softening is unraveled by combining in-situ TEM nanomechanical testing with automated crystal orientation mapping in TEM and high resolution TEM. The softening is attributed to the presence of a high density of stacking faults and of Shockley partial dislocations after hydrogen loading. The hydrogen induced defects affect the elementary plasticity mechanisms and the mechanical response by acting as preferential sites for twinning/detwinning during deformation. These results are analyzed and compared to previous experimental and simulation works in the literature. This study provides new insights on the effect of hydrogen on the atomistic deformation and cracking mechanisms as well as on the mechanical properties of nanocrystalline thin films and membranes.

Keywords

Nanocrystalline Pd films, Mechanical testing, ACOM-TEM, Stacking faults, Electron microscopy

I. Introduction

Owing to its fast and reversible hydriding kinetics, palladium (Pd) is an ideal model system to study the effect of hydrogen (H) absorption. This is essential for hydrogen energy technology, one of the cleanest alternatives to fossil fuels as well as for purification and sensing applications. Pd has a high sensitivity and selectivity with respect to hydrogen and can release hydrogen at room temperature[1,2]. Recently, nanocrystalline (nc) Pd thin films have been widely used in hydrogen applications because of large surface and subsurface site densities and of the presence of a high fraction of grain boundaries (GBs) which can facilitate the hydriding process[3,4]. However, these layers must be thin enough to ensure high hydrogen permeability while remaining mechanically sound and sufficiently ductile[5,6].

The crystalline structure of Pd is face centered cubic (fcc), also referred to as the α-phase. Interstitial hydrogen atoms occupy part of the octahedral sites of the α-phase. During hydriding, as long as the H/Pd ratio stays below α_{SSmax} ~ 0.02 (atomic ratio) at room temperature, the fcc α-Pd lattice parameter can expand from 3.889 Å to 3.895 Å. When the H/Pd ratio reaches 0.02, the so-called β-phase appears with a lattice constant near 4.025 Å. The β-phase exhibits an fcc structure as well. The two phases coexist up to a ratio H/Pd β_{SSmin} ~ 0.58 at which the α phase entirely disappears. The initial volume of the Pd structure expands by about 10% when the H/Pd ratio reaches a value close to 0.5. This dilatation can generate extremely large overall compressive stresses if the deformation is impeded by a mechanical constraint, such as in the case of a film lying on a thick substrate. If the hydrided material is unconstrained, large local stress variations can also take place if the transformation does not occur homogeneously as a result of the diffusion process. The large local or overall stress levels can induce severe local or global plastic deformation, respectively[2,4,6–11]. Hence, it can be expected that the hydriding-induced defects could play a pivotal role in dictating the elementary deformation/failure mechanisms and the mechanical response of the films when subjected to external mechanical loadings.

In the literature, numerous experimental works have been dedicated to the study of the effect of hydrogen on the microstructure and mechanical properties of bulk coarse-grained materials[5,11–16]. However, although nc materials are often considered as promising systems with demonstrated or potential ultra-high structural performances, in-depth experimental investigations on the impact of hydrogen on the mechanical behavior and the small-scale plasticity mechanisms can hardly be found in the literature. Because of the complexity of the microstructure of nc metals, the small-scale plasticity mechanisms may strongly differ from coarse grained metals. Indeed, in nc metals, depending on the grain size and the local stress state, the nucleation of leading partial dislocations from GBs or the production of deformation twins can be favored over the formation of full lattice dislocations even in metals with a high stacking fault energy (SFE)[17]. Furthermore, GB processes such as grain growth, GB sliding and grain rotation can be easily activated at room temperature[18–20].

Very recently, Amin-Ahmadi *et al*. performed extensive TEM characterizations of the nanoscale defect mechanisms activated during hydriding/dehydriding cycles in sputtered nanocrystalline Pd films[3]. The results have shown that, despite the small grain size, local plasticity was mainly controlled by dislocation activity in Pd films hydrided to the β-phase. No clear changes of the grain size distribution and of the crystallographic texture have been observed. Surprisingly, a high density of Shockley partial dislocations (SPDs) and stacking faults (SFs) has been observed after dehydriding, indicating that the presence of hydrogen leads to a decrease of the nucleation energy barriers of SPDs which was confirmed using ab-initio calculations[3]. Defects observed after dehydriding involved wide SFs connected to grain boundaries and delimited by leading SPDs, narrowly dissociated dislocations involving leading and trailing SPDs as well as nanosized shear type glissile SF loops. Their presence in such a high SFE metal after dehydriding was attributed to large internal stress heterogeneities, typical of nc materials[3], or to the presence of neighboring defects. The presence of residual hydrogen atoms at the SPDs core or SFs, which can stabilize these defects after dehydriding, was excluded based on spatially resolved EELS measurements. No residual hydrogen atoms were detected on grain boundaries after dehydriding. In continuation of the work of Amin-Ahmadi *et al*.[3], the present study is focusing on the effect of the hydriding induced SFs and SPDs on

the nanoscale plasticity mechanisms and mechanical behavior of thin nanocrystalline Pd films. More precisely, Pd films subjected to a hydriding/dehydriding cycle to the β-phase were characterized using nanoindentation and advanced TEM techniques including in-situ high resolution TEM nanomechanical testing and automatic crystallographic orientation mapping in TEM (ACOM-TEM).

II. Materials and methods

Nc Pd films were sputter-deposited at room temperature on top of a Si substrate with a deposition rate of 0.3 nm/s and an Argon plasma pressure of 1.07 Pa until a thickness of 150 nm was reached. Earlier work performed on these films by Amin-Ahmadi *et al*.[3] shows an initial microstructure with a lateral grain size of 61 ± 20 nm, while texture analysis reveals a strong {111} preference normal to the film substrate. Hydriding/dehydriding cycles were performed in a vacuum chamber with a pressure lower than 10^{-6} mbar, by instantaneously introducing an ultra-pure Ar/H_2 gas mixture to impose a total pressure of P_{H2} = 2.3 mbar or P_{H2} = 97.5 mbar. As such, the samples were completely hydrided to either α or β phase, respectively[21]. The internal stress was measured in-situ during hydriding with a high-resolution curvature measurement setup mounted on the hydriding chamber (Figure 1). The surface curvature of the cantilevered sample changes due to hydrogen-introduced expansion, which can be monitored in real time using the position of multiple laser beams reflecting off the film[2]. After hydriding, the gas mixture was pumped out of the chamber, resulting in a gradual decrease of the internal stress due to room temperature dehydriding (Fig. 1b). The system returns to ambient conditions. The film is then removed from the hydriding chamber. During hydrogen loading to β phase, the internal stress experienced by the film at equilibrium (~920 MPa, Fig. 1b) is significantly higher than the macroscopic yield stress of the same film (~580 MPa)[17] allowing the generation of dislocations and stacking faults[3]. After a few weeks, in order to study the effect of these hydriding induced defects on the hardness and Young's modulus, nanoindentation experiments were performed under atmospheric conditions on the films subjected to a complete hydriding/dehydriding cycle as well as on reference non hydride Pd films. Thus, it can be safely assumed that most or potentially all the hydrogen has left the Pd films before nanoindentation and that the internal stress induced by hydrogen loading is fully released. These measurements have been performed using the continuous stiffness mode (CSM) and the high precision DCM II head (Dynamic contact module) with a Berkovich tip mounted on an Agilent G200 nanoindenter. Young's modulus and hardness of the film have been determined using the Oliver and Pharr method[22]. On each sample, 16 indents have been performed, and modulus and hardness values were recorded at between 10 and 15 nm depth to minimize substrate effects. Roughness measurements using a Bruker Multimode Nanoscope 8 working in medium tapping mode revealed small Rq (~ 2 nm).

ACOM-TEM[23] was combined with in-situ tensile testing in order to investigate the fundamental plasticity mechanisms of as-deposited and post-mortem hydrided Pd films. In the latter, special attention was paid to the role of the pre-existing hydrogen induced SFs and SPDs for the enhancement of deformation twinning. The tensile tests were performed using the PI 95 TEM PicoIndentor instrument and the push-to-pull (PTP) device (Bruker.Inc)[24–26], see also supplementary materials. Cross-sectional TEM specimens were prepared using focused ion beam (FIB) ("lift-out" procedure) a few weeks after the hydriding/dehydriding cycles and

mounted on the PTP. Thus, as for the nanoindentation experiments, most or potentially even all the hydrogen has left the Pd films before in-situ TEM straining. In order to improve the reliability of the ACOM-TEM measurements, efforts were made to minimize the amount of overlapping grains in the tensile specimen by careful thinning. It is also worth noting that, because the original Pd films used in the present work are not freestanding, cross-sectional samples cut by FIB and transferred onto the PTP device include the FIB deposited Pt protective top layer and a part of the Si-substrate (see supplementary materials). Attempts to remove the Pt top layer and the Si bottom layer by FIB resulted in strongly damaged Pd films. Because of the presence of these extra layers, the present work will thus focus on the deformation mechanisms activated in the Pd films rather than interpreting the relationship between these mechanisms and the in-situ measured load-displacement data.

ACOM-TEM was performed in a FEI Tecnai G2 microscope (FEG, 200 kV), equipped with the ASTAR system from Nanomegas. The electron probe size was ~1.5 nm. Electron precession with an angle of 0.4° was used to minimize dynamical effects and facilitate the automatic indexation of the diffraction patterns[27]. Post-treatment of the data including noise reduction, statistical analysis and interface mapping was achieved with the orientation imaging microscopy (OIM) analysis software from EDAX. A standard EBSD cleanup procedure is applied to this data to correct non-indexed or mis-indexed points. Furthermore, grains with a low reliability (<10%) and smaller than 15 pixels were removed from the analysis. Finally, in-situ high resolution TEM (HRTEM) tests using the PI 95 TEM PicoIndentor and the PTP were performed in a FEI Osiris microscope (FEG, 200 kV) in order to observe in-situ individual dislocation behavior at the nanoscale.

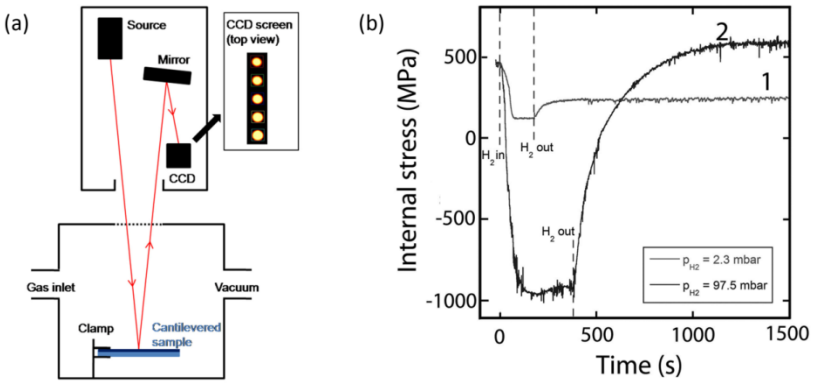

Figure 1: (a) High-resolution in-situ curvature measurement set-up mounted on a hydriding chamber and (b) Typical internal stress evolution during hydriding to α (2.3 mbar) and β-phase (97.5 mbar).

III. Results and discussion

1. Nanoindentation

The effect of hydrogen charging on the mechanical response of the Pd films has been quantified by nanoindentation. The bar chart of Figure 2 compares the hardness of the as-

deposited Pd film as well as of films hydrided at 2.18 mbar (α-phase) and 97.5 mbar (β-phase), see supplementary materials for hardness-displacement curves. The hydrogen loading to the β-phase induces a significant softening compared to the as-deposited film while no difference is observed for a film hydrided to α-phase. As mentioned in the introduction, TEM observations made by Amin-Ahmadi *et al*.[3] revealed a clear increase of the dislocation density and the presence of SFs and SPDs in films hydrided to β-phase while significant changes of the microstructure were not detected in films hydrided to α-phase. The following section will thus focus on the TEM investigation of the deformation mechanisms activated in as-deposited and β-hydrided films. The Young's modulus of the as-deposited (resp. β-hydrided) film estimated by nanoindentation is equal to 98±10 GPa (resp. 83±9 GPa).

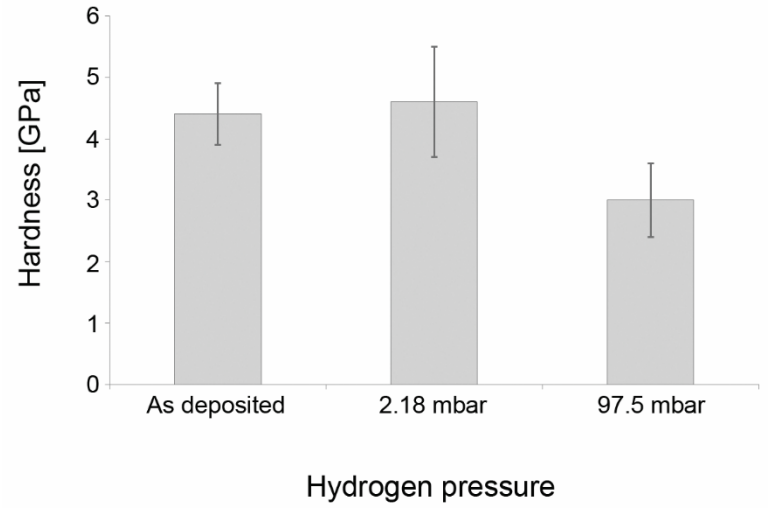

Figure 2: Hardness measurements by nanoindentation in as-deposited films, films hydrided at 2.18 mbar (α phase) and at 97.5 mbar (β phase).

2. In-situ ACOM-TEM mechanical testing

Figure 3a and Figure 3b show ACOM-TEM maps of ∑3 twin boundaries (TBs) in a β-hydrided film respectively before deformation and after an in-situ TEM tensile loading-unloading cycle up to 30 µN. The deformation was performed in the load-control mode with a loading rate of 0.5 µN/s. Index 1 in Figure 3a and Figure 3b indicates the transformation of a GB into a TB which can be explained by grain rotation. This can be concluded both from the change of misorientation angle from 35° to 56° and from the change observed in the inverse pole figures (see Figure 3c and Figure 3d), where, after deformation, a common plane exists between a pair of {111} reflections of the two grains. The combination of this common plane and of a misorientation angle of 60°±9° is maintained for all TBs recognized with ACOM-TEM, following the Brandon criteria for Σ3 {111} CSL boundaries[28,29]. In the literature, nc fcc metals with a medium to high SFE tend to deform by twinning[30]. GBs could transform into TBs by grain rotation in order to minimize their interfacial energy. Indeed, Olmsted *et al*. have shown using atomistic simulations on Ni that Σ3 boundaries tend to have a smaller energy in comparison to other GB types[31]. In the present work, grain rotation induced twinning can be enhanced by local changes of the GB structure due to the accumulation of dislocations at the GB[17,32]. Indeed, Amin-Ahmadi *et al*. have reported a loss of the coherency of Σ3 {111} CTBs in Pd films after hydriding/dehydriding cycles to β phase due to the storage of dislocations at these

boundaries. β hydrides and the associated misfit dislocations are also expected to nucleate and to grow at GBs. The dislocations can be incorporated inside the GB (intrinsic GB dislocations) or accumulate near the GB forming extrinsic GB dislocations. Both features could affect the GB processes by changing its initial structure, orientation and energy.

Indices 2 and 3 in Figure 3a and Figure 3b show the disappearance, after deformation, of nanotwins connected to GBs, leading to a bigger grain. Such behaviour can be explained by the nucleation and the glide of de-twinning dislocations with b=1/6 <112> at the CTB/GB sites[30,33]. It has been shown by Li *et al*. using atomistic simulations on nc Cu, that below a certain twin thickness a dislocation-nucleation controlled softening mechanism occurs due to the nucleation and motion of partial dislocations parallel to the twin plane[33]. At index 4 in Figure 3a and Figure 3b, twin expansion due to the migration of Σ3{112} incoherent TB (ITB), connecting two parallel Σ3{111} coherent TB (CTB) can be clearly seen. A schematic illustration of this phenomenon is provided in Figure 3e and Figure 3f. Σ3 {112} ITBs can migrate under moderate applied stress, causing twin expansion[4,34]. Such behaviour could also explain the detwinning behaviour shown in indices 2 and 3 due to the nucleation and backward motion of Σ3{112} ITBs. Indeed, Σ3{112} ITBs can be formed by the dissociation of high energy GBs into Σ3{111} CTB and Σ3{112} ITB in order to decrease the total interfacial energy. It is important to note here that similar intense twinning/detwinning activity was not observed in as-deposited Pd films deformed in identical conditions. Such behaviour can be attributed to the microstructural changes in the β hydrided films including: i) changes of the structure/energy of GBs due to dislocation/GB interactions, which could lead to grain rotation induced twinning as well as the dissociation of GBs into CTBs and ITBs as shown in Figure 3. ii) the presence of the hydrogen induced SFs and SPDs that can act as preferential sites for twinning upon deformation. The latter was confirmed using in-situ HRTEM tensile testing as will be shown in the following section.

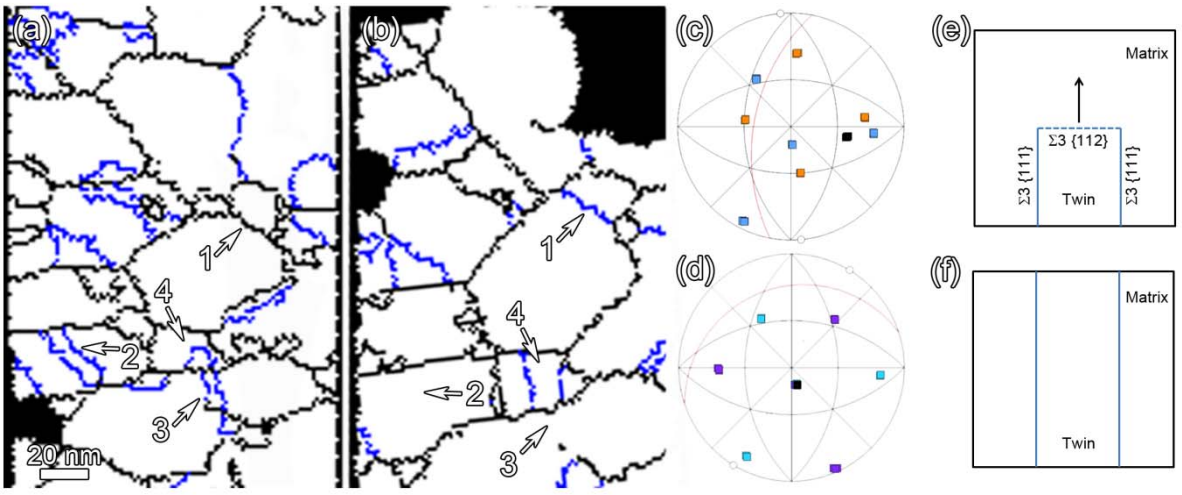

Figure 3: TB map of the Pd film hydrided to β phase (a) before deformation and (b) after in-situ loading-unloading cycle up to 30 µN. Blue lines indicate Σ3 CSL twin boundaries while the black lines highlight the position of all other possible GBs. Arrows with according numbers were added to both figures in order to indicate changes in twinning behaviour after deformation. (c) Pole figures from the GB marked as index 1 before deformation and (d) after

deformation. In each pole figure, the two colour codes of the squares represent the different orientations of the neighboring grains while the black square indicates the common plane, wherein a pair of {111} reflections of the two grains perfectly overlap after deformation. (e,f) Schematic illustration of twin expansion due to the motion of Σ3{112} ITB in the grain with index 4, respectively.

3. In-situ HRTEM mechanical testing

In Figure 4a, a growth nanotwin with two parallel CTBs connected to a GB can be observed in the β (de)hydrided sample. A widely dissociated dislocation induced by hydriding to β phase is indicated by white arrowheads close to the upper CTB in Figure 4a. As described in the introduction, such wide SFs have not been observed by Amin-Ahmadi *et al*. in as-deposited Pd films[3]. SFs were neither observed in Pd films hydrided to α phase (low H pressure)[3] which has been attributed to the small amount of hydrogen incorporated in the lattice and the low stress levels reached during this hydriding cycle (Figure 1b). During the in-situ tensile straining, SFs were observed to form at the CTBs (Figure 4b). This leads to a decrease of the thickness of the twin (i.e., detwinning) as can be seen in the same figure. CTB migration involving the nucleation and glide of new twinning dislocations at the CTB/GB intersection sites has been reported before[30,33]. Such behaviour can be enhanced in the present work due to the storage of dislocations at GBs during hydriding to β phase as well as the presence of pre-existing hydrogen induced SFs (Figure 4a) that can act as preferential sites for the nucleation of new SFs as will be seen below.

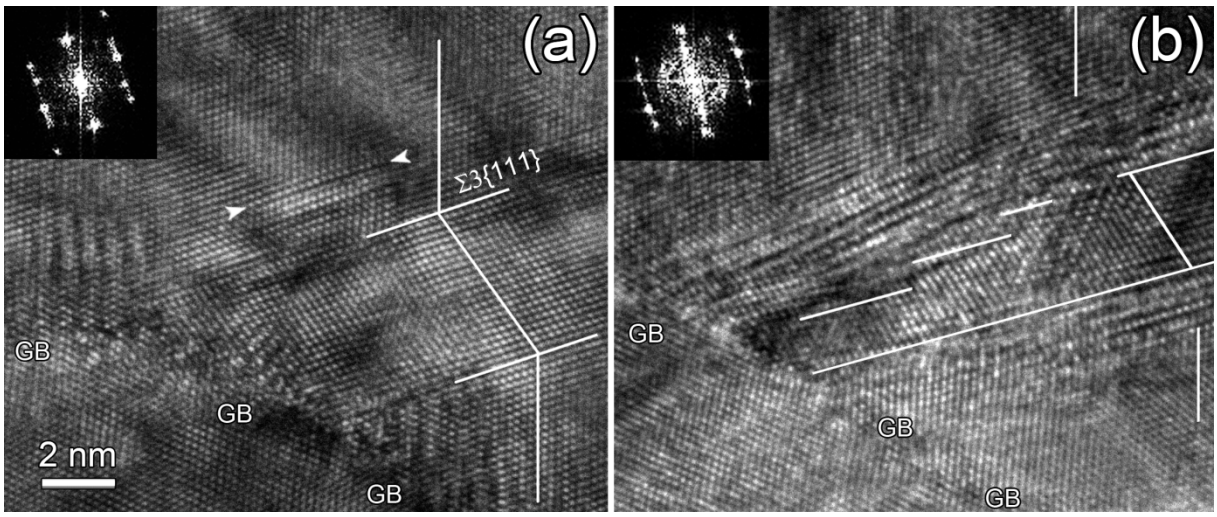

Figure 4: HRTEM images of the β (de)hydrided Pd film (a) before deformation and (b) after the tensile cycle up to 160 µN. A widely dissociated dislocation with a central SF and induced by hydriding to β phase is highlighted with white arrowheads in (a) while the FFT of both images is provided in their respective top left corner.

The HRTEM image of Figure 5a shows two stacking faults (SF1 and SF2) connected to a GB in the Pd film hydrided to β phase, before deformation. Figure 5b exhibits the change of the stacking sequence of the {111} planes due to the presence of the single SF2 while Figure 5c exhibits a local g-map showing the position of the leading partial dislocation delimiting this SF. The HRTEM image of Figure 5d was acquired after a loading-unloading cycle up to 160µN. It

shows that SF1 has disappeared due to the backward motion of the SPD delimiting this SF towards the GB. However, SF2 transformed into a nanotwin as confirmed by the FFT displayed in the top right inset of the same figure. This is obtained by the successive formation of new twinning dislocations from the GB/SF interaction site. The difference between the behaviour of SF1 and SF2 is probably due to the different sign of their Burgers vectors with respect to the external applied stress. Using atomistic simulations Stukowski *et al*. reported that in pure Pd with pre-existing SFs softening occurs due to the nucleation of new partial dislocations parallel to the SF plane[35]. The presence of a SF decreases the energy barrier for twinning by facilitating the formation of a second SF in the plane immediately adjacent to the first SF. It is also worth noting that, although the observations shown in Figure 5 have been performed in a single grain, the effect of the hydrogen induced SFs and SPDs on twinning/detwinning is expected in all the grains since Amin-Ahmadi *et al*. reported a high density of these defects homogenously distributed within all the analyzed grains.

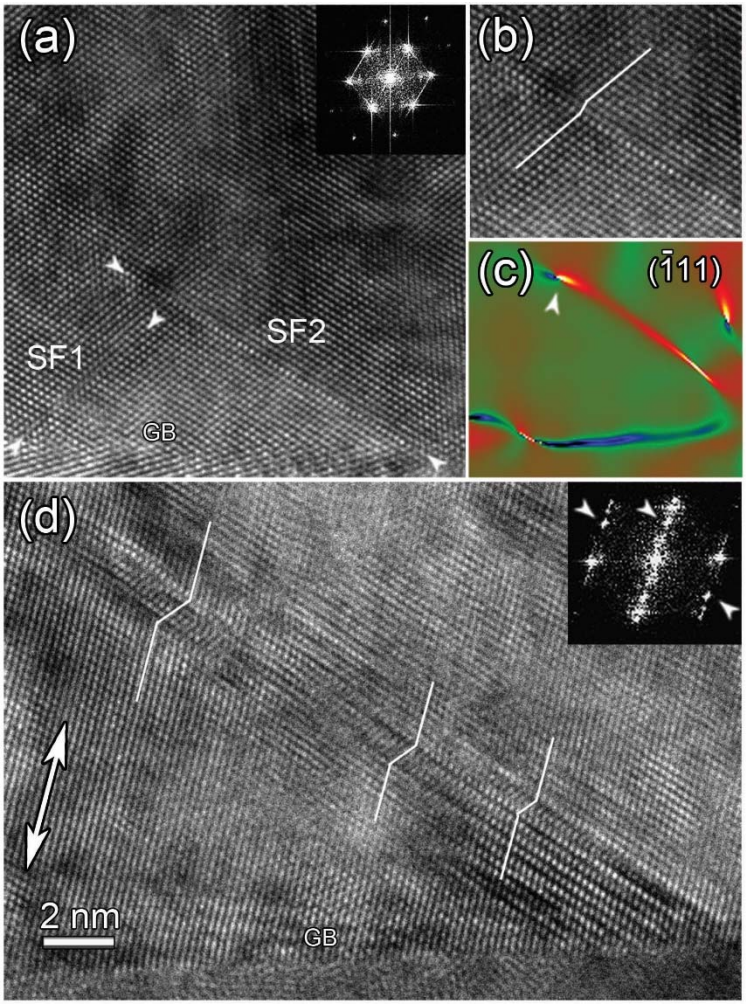

Figure 5: (a) SFs (1, 2) formed close to a GB and indicated by arrowheads. The FFT is shown in the inset. (b) Enlarged image of SF2 in (a), (c) local g-map of the $(\bar{1}11)$ plane with an arrowhead indicating the position of the SPD delimiting SF2 as a hot spot. (d) Deformation twin formed from SF2 after the loading/unloading cycles up to 160µN. Extra twinning reflections are highlighted with arrowheads in the FFT shown in the inset. The tensile axis is indicated by the double arrow in (d). The white lines in (d) indicate changes of the stacking sequence of the $(\bar{1}11)$ plane due to the presence of twinning dislocations.

The results of the in-situ ACOM-TEM and HRTEM analysis confirm that SFs and SPDs induced by hydriding to β phase could play an important role in the plasticity by acting as sources not only for deformation twinning (Figure 5) but also for detwinning (Figure 4). This also explains the softening behaviour observed in Figure 2. Indeed, several experimental investigations and simulations have attributed mechanical softening in nc materials to twinning and partial dislocation dominated plasticity[33,35]. Very recently, Y. Zhao *et al*. investigated the effect of hydrogen charging on the plastic deformation of nc Ni using nanoindentation[36]. The results revealed an hydrogen-induced softening behaviour that was explained by hydrogen-enhanced activity of partial dislocations emitted from GBs and/or abundant hydrogen-vacancy cluster formation around GBs. However, nanoscale characterizations of the deformed microstructure were not performed to validate such features. The present work thus provides first of kind experimental evidences on the role of partial dislocations in softening of hydrided nc metallic films. Hydrogen-vacancy cluster formation around GBs can be excluded based on the earlier spatially resolved EELS measurements performed on GBs and dislocations by Amin-Ahmadi *et al*. Since the absence of residual hydrogen atoms at the defects has been confirmed based on EELS[3], a possible impact on the small-scale plasticity mechanisms observed with in-situ TEM can be excluded. However, its contribution to the softening behavior observed in nanoindentation experiments cannot be totally excluded as these measurements have been performed on samples not affected by the FIB or electron exposure.

IV. Conclusions

The effect of SPDs and SFs induced by hydriding/dehydriding cycles to β phase on the mechanical response and the nanoscale plasticity mechanisms in nc thin Pd films has been investigated using nanoindentation and in-situ TEM nanomechanical testing. The in-situ HRTEM observations revealed that the pre-existing SFs act as preferential sites for twinning/detwinning in agreement with the in-situ ACOM-TEM observations. The latter also revealed the activation of grain rotation induced twinning and the dissociation of GBs into Σ3{111} CTB and Σ3{112} ITB followed by the migration of the ITBs. Such features were attributed to changes of the local structure/energy of GBs after hydrogen loading due to the storage of dislocations at GBs. The origin of these dislocations can be attributed to the nucleation of dislocations from GBs or intra-granular sources (due to the build-up of the internal stress during β hydriding) as well as the preferential formation of the β hydrides and the resulting misfit dislocations on GBs. The observed partial dislocation dominated plasticity and GB processes could explain the softening observed in the β hydrided films compared to the as-deposited films, as revealed by nanoindentation.

V. Supplementary Material

The PI 95 TEM PicoIndentor holder from Bruker Inc. with a conductive diamond flat punch indentor was used to perform load-controlled compression. To convert the compressive force to a tensile force, the sample was mounted on a push-to-pull (PTP) chip (Figure S1a). This device is a special microelectromechanical system which contains four identical springs mounted in the corners of the system and arranged parallel to the indentation direction. The diamond tip compresses the semicircular end of the PTP device, inducing a uniaxial tensile

loading over the middle gap of the PTP device. In this experiment, the stiffness of the springs was equal to 450 N/m.

For sample preparation, a FEI Helios dual beam FIB/SEM instrument was used to cut the Pd thin film as cross-sectional samples, including the FIB deposited Pt protective layer and a part of the Si substrate. Using a build-in Omniprobe micromanipulator, the sample was transferred to the middle gap of the PTP device (Figure S1b) and attached with electron-beam deposited Pt. Thus, in order to obtain thin Pd samples for ACOM and HRTEM, careful thinning was performed with FIB on the PTP. Figure S1c shows an example of a loading-unloading cycle up to 30 µN during the in-situ experiment.

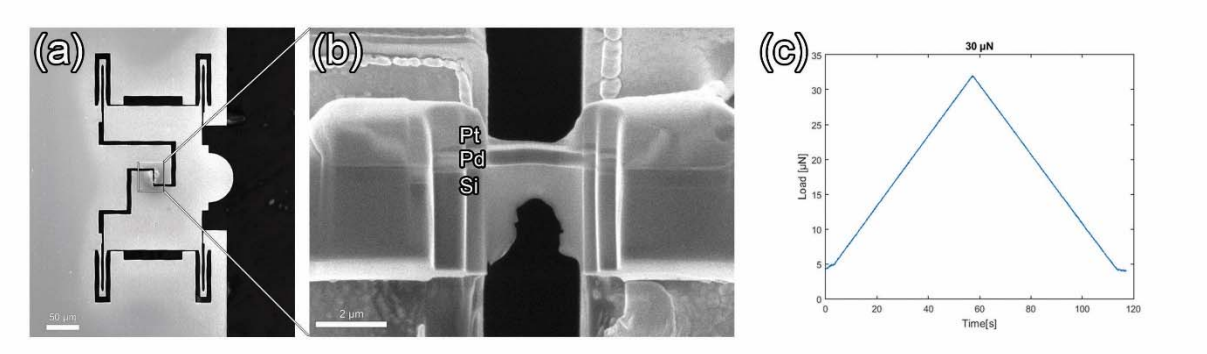

Figure S1: (a) Low magnification SEM image of the PTP chip. The FIB sample is mounted over the highlighted middle gap and shown in (b) at a higher magnification. (c) Load-unloading cycle up to 30 µN.

Usual rule of thumbs in nanoindentation testing suggests that for a reliable measurement, roughness should represent less than 5 % of the indentation depth. Here, the hardness values are taken between 10 and 12% of the film thickness in order to avoid substrate effect, i.e. between 15 and 18 nm, which is a little less than the above-mentioned rule. Nevertheless, roughness mainly induces scatter in the measurements, which is taken into account by the confidence interval. The additional figure provided as supplementary material (figure S2) shows that the conclusions are still valid despite of the larger scatter. Moreover, the relative position of the hardness values of the different samples does not change even if the hardness is considered at larger depths so as to fulfil the rule indicated above.

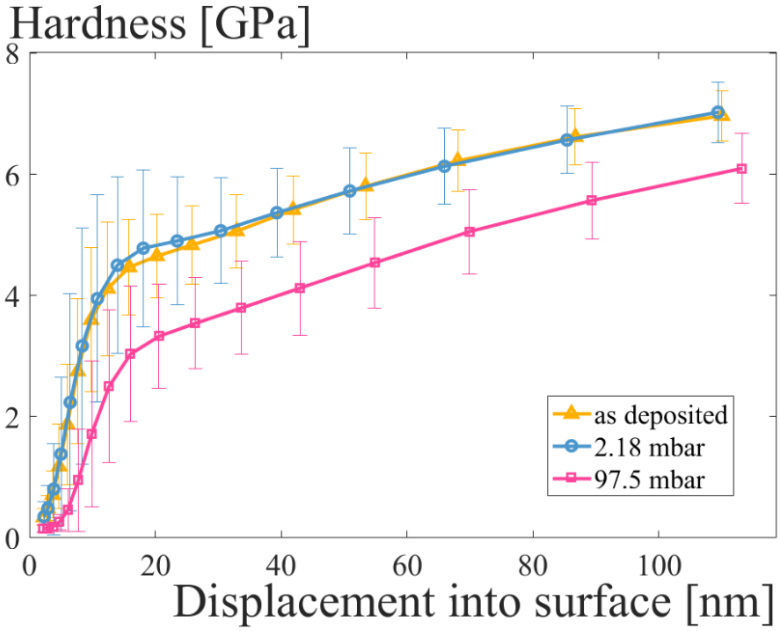

Figure S2: Hardness-displacement curves of the nanoindentation experiments performed under atmospheric conditions on the films subjected to a complete hydriding/dehydriding cycle as well as on reference non hydride Pd films.

Acknowledgements

This work was supported by the Hercules Foundation under Grant AUHA13009; the Flemish Research Fund (FWO) under Grant G.0365.15N; and the Flemish Strategic Initiative for Materials (SIM) under the project *InterPoCo*. Dr. H. Idrissi is mandated by the Belgian National Fund for Scientific Research (FSR-FNRS). We would like to thank dr. Hadi Pirgazi from UGent for his technical support to process the ACOM data in the OIM Analysis software.

References

1. K.L. Salcedo, C.A. Rodríguez, F.A. Perez and H. Riascos, J. Phys. Conf. Ser. **274,** (2011).

2. R. Delmelle, G. Bamba and J. Proost, Int. J. Hydrogen Energy **35,** 9888 (2010).

3. B. Amin-Ahmadi, D. Connétable, M. Fivel, D. Tanguy, R. Delmelle, S. Turner, L. Malet, S. Godet, T. Pardoen, J. Proost, D. Schryvers and H. Idrissi, Acta Mater. **111,** 253 (2016).

4. B. Amin-Ahmadi, H. Idrissi, R. Delmelle, T. Pardoen, J. Proost and D. Schryvers, Appl. Phys. Lett. **102,** 071911 (2013).

5. V. Bérube, G. Radtke, M. Dresselhaus and G. Chen, Int. J. energy Res. **31,** 637 (2007).

6. H. Kou, J. Lu and Y. Li, Adv. Mater. 26, 5518 (2016).

7. E.M. Salomons, R. Feenstra, D.G. De Groot, J.H. Rector and R. Griessen, J. Less-Common Met. **130,** 415 (1987).

8. H. Gleiter, Adv. Mater. **4,** 474 (1992).

9. M.V. Goltsova and G.I. Zhirov, Met. Sci. Heat Treat. **49,** 141 (2007).

10. T.B. Flanagan and W.A. Oates, Annu. Rev. Mater. Sci. **21,** 269 (1991).

11. R. Delmelle, B. Amin-Ahmadi, M. Sinnaeve, H. Idrissi, T. Pardoen, D. Schryvers and J. Proost, Int. J. Hydrogen Energy **40,** 7335 (2015).

12. J.M. Wheeler and T.W. Clyne, Int. J. Hydrogen Energy **37,** 14315 (2012).

13. E. Dillon, G. Jimenez, A. Davie, J. Bulak, S. Nesbit, A. Craft, Mater. Sci. Eng. A **524,** 89 (2009).

14. M.V. Goltsova, Y.A. Artemenko and V.I. Zaitsev, J. Alloys Compd. **293,** 379 (1999).

15. G. Jimenez, E. Dillon, R. Miller, F. Massicotte, S. Nesbit and A. Craft, Scr. Mater. **59,**

870 (2008).

16. G. Jimenez, E. Dillon, J. Dahlmeyer, T. Garrison, T. Garrison, S. Darkey, K. Wald, J. Kubik, D. Paciulli, M. Talukder, J. Nott, M. Ferrer, J. Prinke, P. Villaneuva, F. Massicotte, K. Rebeiz, S. Nesbit, and A. Craft, Adv. Chem. Eng. Sci. **6,** 246 (2016).

17. B. Wang, H. Idrissi, M. Galceran, M.S. Colla, S. Turner, S. Hui, J.P. Raskin, T. Pardoen, S. Godet and D. Schryvers, Int. J. Plast. **37,** 140 (2012).

18. A. Kobler, J. Lohmiller, J. Schäfer, M. Kerber, A. Castrup, A. Kashiwar, P.A. Gruber, K. Albe, H. Hahn and C. Kübel, Beilstein J. Nanotechnol. **4,** 554 (2013).

19. F. Mompiou and M. Legros, Scr. Mater. **99,** 5 (2015).

20. Y. Ivanisenko, N.A. Enikeev, K. Yang, A. Smoliakov, V.P. Soloviev, H. Fecht and H. Hahn, Mater. Sci. Eng. *A* **668,** 255 (2016).

21. R. Delmelle, S. Michotte, M. Sinnaeve and J. Proost, Acta Mater. **61,** 2320 (2013).

22. W.C. Oliver, and G.M. Pharr, J. Mater. Res. **19,** 3 (2004).

23. E.F. Rauch and M. Véron, Mater. Charact. **98,** 1 (2014).

24. A. Kobler, A. Kashiwar, H. Hahn and C. Kübel, *Ultramicroscopy* **128,** 68 (2013).

25. H. Idrissi, C. Bollinger, F. Boioli, D. Schryvers and P. Cordier, Sci. Adv. **2,** 1 (2016).

26. H. Idrissi, A. Kobler, B. Amin-ahmadi, M. Coulombier, M. Galceran, J.P. Raskin, S. Godet, C. Kübel, T. Pardoen and D. Schryvers, Appl. Phys. Lett. **104,** 101903 (2014).

27. A. Kobler and C. Kübel, Ultramicroscopy **173,** 84 (2017).

28. D.G. Brandon, Acta Metall. **14,** 1479 (1966).

29. A.F. Acton and M. Bevis, Acta Crystallogr. Sect. A **27,** 175 (1971).

30. Y.T. Zhu, X.Z. Liao and X.L. Wu, Prog. Mater. Sci. **57,** 1 (2012).

31. D.L. Olmsted, S.M. Foiles and E.A. Holm, Acta Mater. **57,** 3694 (2009).

32. H. Idrissi, B. Wang, M.S. Colla, J.P. Raskin, D. Schryvers and T. Pardoen, Adv. Mater. **23,** 2119 (2011).

33. X. Li, Y. Wei, L. Lu, K. Lu and H. Gao, Nature **464,** 25 (2010).

34. H. Idrissi, B. Amin-Ahmadi, B. Wang and D. Schryvers, Phys. Status Solidi Basic Res. **251,** 1111 (2014).

35. A. Stukowski, K. Albe and D. Farkas, Phys. Rev. B - Condens. Matter Mater. Phys. **82,** 1 (2010).

36. Y. Zhao, M.Y. Seok, D.H. Lee, J.A. Lee, J.Y. Suh, and J.I. Jang, Philos. Mag. **96,** 3442–3450 (2016).